catalysts

MDPI

Communication

Dual Metal Site Fe Single Atom Catalyst with Improved Stability in Acidic Conditions

Yuehua Wang [1,†], Shuang Li [2,†], Rui Xu [2,†], Junpeng Chen [2], Yifan Hao [2], Ke Li [2], Yan Li [2], Yingmei Li [1,*] and Jing Wang [1,2,*]

[1] State Key Laboratory of Metastable Materials Science and Technology, Yanshan University, Qinhuangdao 066004, China
[2] Hebei Key Laboratory of Heavy Metal Deep-Remediation in Water and Resource Reuse, School of Environmental and Chemistry Engineering, Yanshan University, Qinhuangdao 066004, China
* Correspondence: liyingmei@ysu.edu.cn (Y.L.); jwang6027@ysu.edu.cn (J.W.)
† These authors contributed equally to this work.

Abstract: Dual atom catalysts (DACs) not only retain uniform active sites and high atomic utilization efficiency as the single atom catalysts, but the two adjacent metal sites also cooperate and play a synergistic role to achieve additional benefits. However, the relationships connecting their dual-site synergistic effects on catalytic performance are not well rationalized due to limited pairs available from experiments. Herein, Fe/M dual sites supported by nitrogen doped carbon (Fe/M-N-C whereby M from 3 d–5 d electron containing transition metals) have been screened as an oxygen reduction reaction (ORR) catalyst. The results show that the absorption strength of ORR intermediates on four nitrogen coordinated metals is weaker than the three coordinated metals, which promotes favourable ORR activities. As a result, we recommended FeIr, FeRh, FeRu and FeOs as promising ORR catalysts. Ab initio molecular dynamic (AIMD) simulations suggest Fe/M-N-C (M = Ir, Rh, Ru and Os) catalysts with encouraging structural stability at room temperature. Furthermore, it is found that the nitrogen atoms in-between metals are vulnerable sites for proton attacking, yet the protonation process demands high energy, even under O_2 atmosphere, which underlines good tolerance under acidic conditions. This work provides a broad understanding of Fe based catalyst and a new direction for catalytic design.

Keywords: iron-based dual-atom catalysts; volcano plot; fuel cell; working condition; synergistic effect

check for updates

Citation: Wang, Y.; Li, S.; Xu, R.; Chen, J.; Hao, Y.; Li, K.; Li, Y.; Li, Y.; Wang, J. Dual Metal Site Fe Single Atom Catalyst with Improved Stability in Acidic Conditions. *Catalysts* **2023**, *13*, 418. https://doi.org/10.3390/catal13020418

Academic Editor: Junfeng Liu

Received: 28 November 2022
Revised: 31 December 2022
Accepted: 4 January 2023
Published: 16 February 2023

Copyright: © 2023 by the authors. Licensee MDPI, Basel, Switzerland. This article is an open access article distributed under the terms and conditions of the Creative Commons Attribution (CC BY) license (https://creativecommons.org/licenses/by/4.0/).

1. Introduction

Advanced energy conversion and storage systems have received considerable attention due to their significant roles in the field of clean energy [1–3]. Among various clean energy technologies, fuel-cells are considered as promising candidates due to their high energy density and eco-friendliness [4,5]. However, slow kinetics of oxygen reduction reaction (ORR) limits the discharge power density of the device, and it is extremely challenging to overcome this obstacle [6,7]. Till now, noble metal-based materials are selected as the commercial electrocatalysts, dominating a large percentage of the fuel-cell market price, which demands the development of cost-effective and high performance non-precious metal catalysts.

Single atom catalyst (SAC) has been proposed to achieve 100% atomic utilization for precious metal [8], and recent studies have mentioned the upsurge of the atomically dispersed transition metal nitrogen doped carbon materials (known as M-N-C, wherein M stands for transition metals), derivatives from the biological systems which have shown great promise in the field of ORR catalysis [9–20]. In particular, well-dispersed Fe-N-C is enabled with competitive catalytic activity as commercial Pt-based catalysts [21–25]. However, Fe-N-C catalyst lacks long-term stability in acid medium, which tends to be involved in various side-reactions, hindering its industrial application in fuel cells.

Dual atom catalysts (DACs), an extension of SACs, are receiving increasing attention due to additional benefits rooted from electronic structure modulation [26–34]. For example, Fe/Co-N-C [26] was first synthesized by an Li group, which exhibited improved catalytic performance compared with its SAC counterparts. Following closely, it was used as a prototype to achieve bifunctional catalysis for both ORR and oxygen evolution energy (OER) [27]. Recently, Fe/Mn-N-C [28] was further demonstrated with excellent ORR performance in both alkaline and acidic media, and the key factors are ascribed to the spin related electronic structure adjustment. A unique half metallic quantum state was reasonably designed as in Fe/Zn-N-C [29] catalyst, which outperformed in both catalytic activity and long-life stability, providing new insights for the development of high-performance electrocatalysts. However, the reaction mechanism is not well rationalized in Fe based DACs due to limited pairs available from experiments, not to mention the structure evolution during working conditions.

In this study, based on systematic density functional theory (DFT) calculations, 13 Fe/M pairs of two distinct configurations are investigated as Fe/M-N-C OERR catalysts, with M covering from 4 d to 6 d transition metals (Cr, Mn, Co, Ni, Cu, Zn, Mo, Ru, Rh, W, Re, Os, and Ir). In addition to the Fe/Co, Fe/Mn, Fe/Ni, Fe/Zn and Fe/Cu which are available from experiments, four new candidates, including Fe/Ir (η = 0.26 V), Fe/Rh (η = 0.30 V), Fe/Ru (η = 0.42 V) and Fe/Os (η = 0.57 V) have been found with satisfied ORR activity, which are thermodynamically stable at 300 K from dynamic simulation. Attractively, the simulation of protonation process gives rise to high free energy demanded for surface hydrogenation, demonstrating improved structure stability in acid conditions.

2. Results and Discussion

Schematic models for $FeMN_6$(I) and $FeMN_6$(II) are shown in Figure 1. In $FeMN_6$(I), two N atoms are shared by metal sites, forming four N coordinated metal centers, yet, in $FeMN_6$(II), each metal is three coordinated with N atoms. In total, 13 metal elements are paired with Fe, yet the configurations of $FeReN_6$(II) and $FeWN_6$(II) are not capable in stabilizing *OOH (Table S1), which is thus beyond the following study for the 4e reaction pathway.

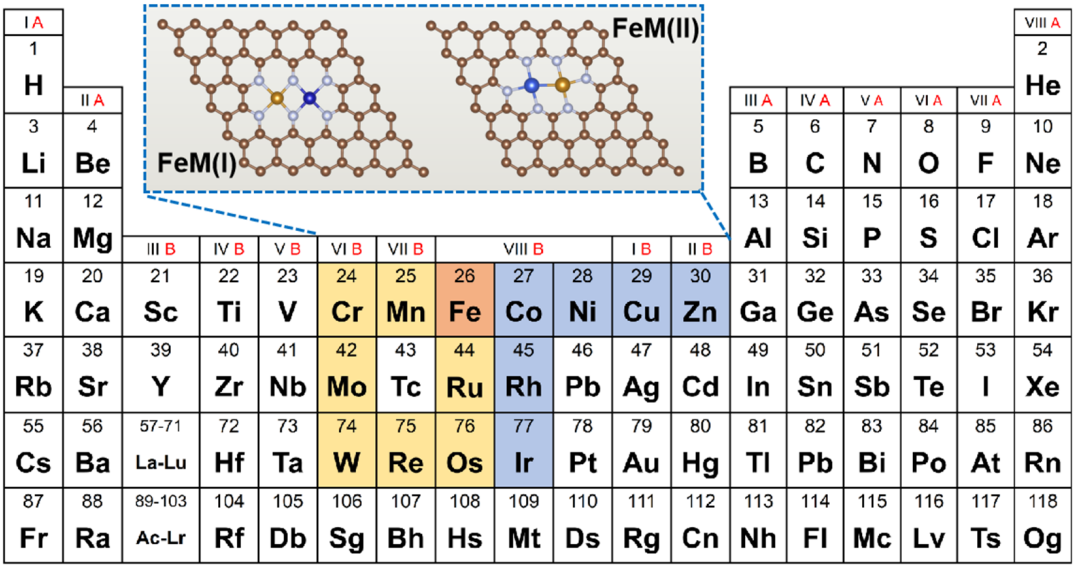


Figure 1. The $FeMN_6$ with two different N coordination configurations, and the selected M atoms are highlighted with yellow, orange, and blue color in the periodic table. Atomic labels in the insert chemical structures: C (brown), N (lavender), Fe (brown), and M (dark blue).

The optimized structures, along with the key reaction intermediates (*O_2, *OOH, *O and *OH), are depicted in Table S1. For the first H^++*e* step of ORR, the capture of O_2

molecules is analyzed by the O_2 adsorption energy, as observed in Figure 2 (Table S2). According to Sabatier's law [35], the ORR catalyst requires moderate adsorption energy for O_2, as strong adsorption will cause the catalyst surface inhabitant by O_2, but weak binding will make it difficult to initiate the catalytic reaction. A favorable O_2 adsorption energy is estimated to be between −0.6~−0.7 eV. [27] Active centers which meet this precondition include $FeCoN_6$(I), $FeNiN_6$(I), $FeRhN_6$(I), $FeOsN_6$(I), $FeRuN_6$(I), and $FeIrN_6$(I), with ΔE_{ads} of −0.63 eV, −0.79 eV, −0.67 eV, −0.78 eV, −0.82 eV, and −0.78 eV, respectively. For a specific metal pair, $FeMN_6$(II) configuration exhibits stronger O_2 absorption ability as evidenced by larger adsorption energy. The calculated ΔE_{ads} values for $FeMN_6$(II) are between −1.5 eV and −4.0 eV, and thus $FeMN_6$(II) is not conducive to a smooth ORR. Here, it is found that the O-O bond is elongated from 1.23 Å in gas-phase to XX in the absorbant as shown in Figure 2, demonstrating that the O_2 is activated. In addition, the elongation of O-O bond is more pronounced in $FeMN_6$(II) than that in $FeMN_6$(I) because of the stronger O_2 adsorption in the former. From the results of Bader Charge (Table S3), it is seen that after the $*O_2$ binding on the metal sites, the oxidation states of Fe are enhanced. This is understandable because the O_2 extracts electrons from metal sites.

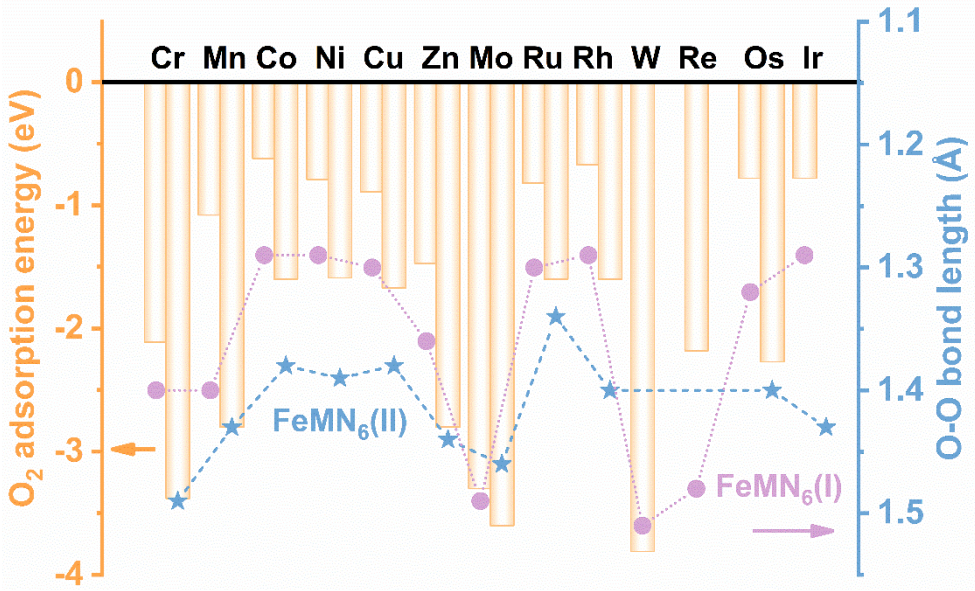


Figure 2. O_2 adsorption energy (ΔE_{*O2}) (yellow bar) and O−O bond length (purple spots and blue star). For each transition metal, the left yellow bar is for $FeMN_6$ (I), and the right yellow bar is for $FeMN_6$ (II).

It is aware that the adsorption sites of O_2 and the adsorption configurations are different (Figure 3). For most $FeMN_6$(I), the $*O_2$ is absorbed on the metal with side-on configuration, where one O interacts with one metal site while the other O points away from the surface (although $*O_2$ adopts end-on configuration in Cr case, other intermediates interact with Cr site, instead of both metals). The following reaction steps proceed with the terminal O atom. The key intermediates (*OH, *OOH, *O) tend to bind to the M site, when M locates on the left of Fe in the period table (M = Cr, Mn, Mo, Ru, W. Re, Os); otherwise, Fe is preferred. By contrast, the two oxygen atoms in the O_2 molecular can interact with both Fe and M atoms in $FeMN_6$(II) (except FeMo couple), so do the *O and *OH species, which well explains the stronger interaction between adsorbates and catalysts.

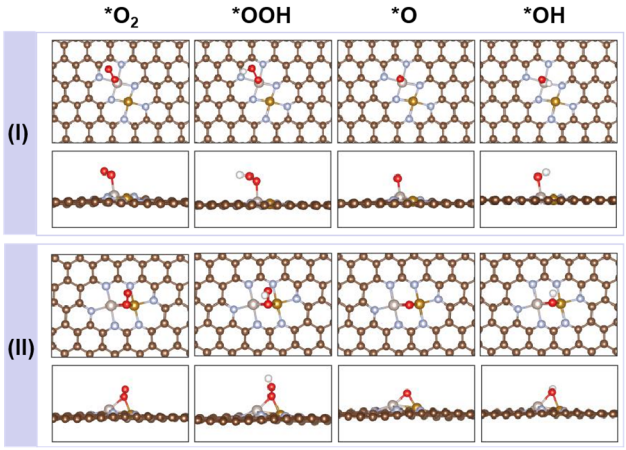


Figure 3. Typical structures for the key oxygen containing intermediates for both $FeMN_6$(I) (top) and $FeMN_6$(II) (bottom), top view and side view.

ORR catalytic activity was assessed by the free energy changes of the key oxygen-containing intermediates, i.e., *OOH, *O and *OH, (Table S4 and Figure S1). The standard equilibrium potential for reaction steps R1–R4 are calculated from the free energy value, as shown in Figure 4 for $FeMN_6$(I) and Figure S2 for $FeMN_6$(II). The ideal reaction free energy value for the elementary step is 1.23. Since each intermediate plays dual roles, namely, the product of the former elementary reaction and the reactant of the following elementary reaction, the variation from the ideal value should be small. In other words, the closer to the standard equilibrium potential value, the better the catalytic activity. It is witnessed that, for $FeMN_6$(I) with FeCo, FeMn, FeCu, FeZn, FeRu, FeRh, FeOs and FeIr pairs, the ΔG values are close to each other, suggesting good activity. Unfortunately, a huge difference in standard equilibrium potential for the elementary steps can be found for all considered $FeMN_6$(II) configurations (Figure S2), excluding potential candidates with satisfied performance.

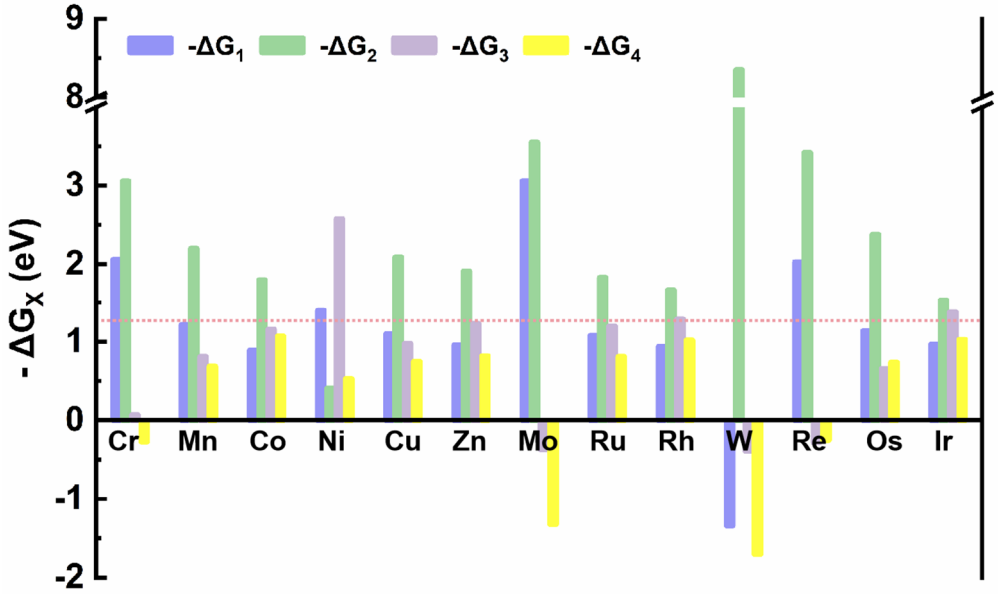


Figure 4. Standard equilibrium potential for reaction steps R1−R4 for $FeMN_6$(I) (M = Cr, Mn, Mo, Ru, W, Re, Os, Co, Ni, Cu, Re, Os, Co, Ni, Cu, Zn, Rh and Ir) moieties. The red dotted line is the ideal reaction free energy at 1.23 eV.

A close inspection of Figure 4 finds out that the lowest ΔG values are in general for the *OH→H_2O step, which corresponds to the desorption of the *OH intermediates.

This suggests that the formation of the second H_2O is the potential determining step (PDS). Therefore, a volcano relationship between the ΔG_{*OH} and the negative catalytic overpotential ($-\eta$) is plotted in Figure 5. It is seen that all $FeMN_6$(II) configurations are located on the left side of the volcano, underlining strong adsorption of *OH, which hampers the further protonation of *OH. On the contrary, most $FeMN_6$(I) configuration sites on the right side are relative to those of $FeMN_6$(II), illustrating alleviate *OH binding. As a result, $FeIrN_6$(I) (η = 0.26 V), $FeRhN_6$(I) (η = 0.30 V), $FeRuN_6$(I) (η = 0.42 V), $FeCoN_6$(I) (η = 0.34 V) and $FeZnN_6$(I) (η = 0.41 V) give smaller overpotential than that of commercial Pt/C (η = 0.45 V) and other Fe based dual site counterparts (Table S5). In addition, the overpotential of $FeOsN_6$(I) (η = 0.57 V), $FeCuN_6$(I) (η = 0.48 V) and $FeMnN_6$(I) (η = 0.54 V) is also small, holding great promise for high activity reaction centers.

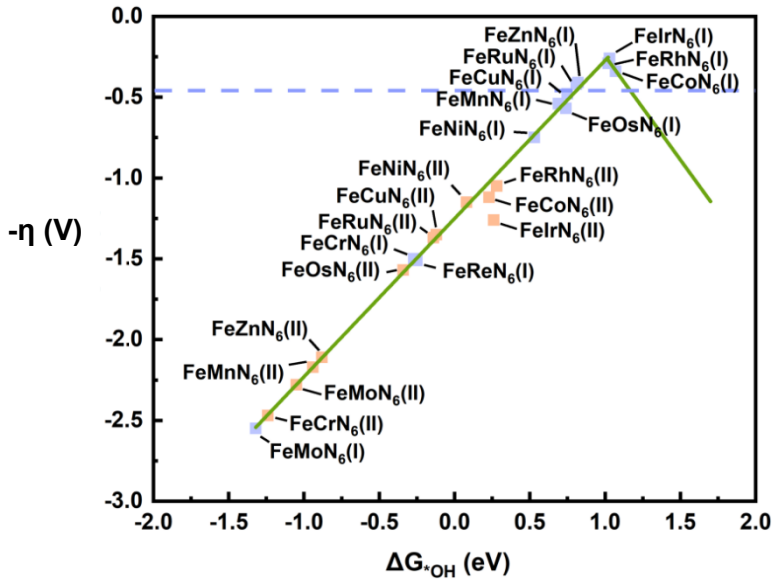


Figure 5. Volcano plot of $-\eta$ related to ΔG_{*OH} for $FeMN_6$(I) and $FeMN_6$(II).

Among these reaction centers, the combinations of FeCo, FeMn, FeCu and FeZn are available from experiments, which exhibit excellent ORR performance, in accordance with our work. However, for $FeRuN_6$(I), $FeRhN_6$(I), $FeIrN_6$(I) and $FeOsN_6$(I), which are excluded from current experiments, AIMD simulation is performed to address their stabilities (Figure S3). It is seen that the total energy oscillates in a small range within 10 ps at 300 K, indicating solid stability kinetically. Moreover, the active center and carbon skeleton of the catalyst are remained as in the initial configuration (inset of Figure S3), another piece of evidence for the high stability.

Besides reaction activity, the structure stability under working condition is also an important criterion for a good catalyst. When operating in the cathode of a fuel cell, the catalyst is exposed under acid conditions, the attacking of H^+ in the reaction center will cause the structure degradation and the change of the electronic structure. Therefore, the protonation is simulated for the screened $FeRuN_6$(I), $FeRhN_6$(I), $FeIrN_6$(I) and $FeOsN_6$(I) reaction centers with one and two protons adsorbed on the surface. It is revealed that the shared N sites are favorable for binding *H (Figure 6 and Table S6), yet the positive free energy change demonstrates that the protonation process is endothermic. Moreover, compared with the first *H binding, the energy demanded for another *H is higher, indicating good tolerance in acid environments.

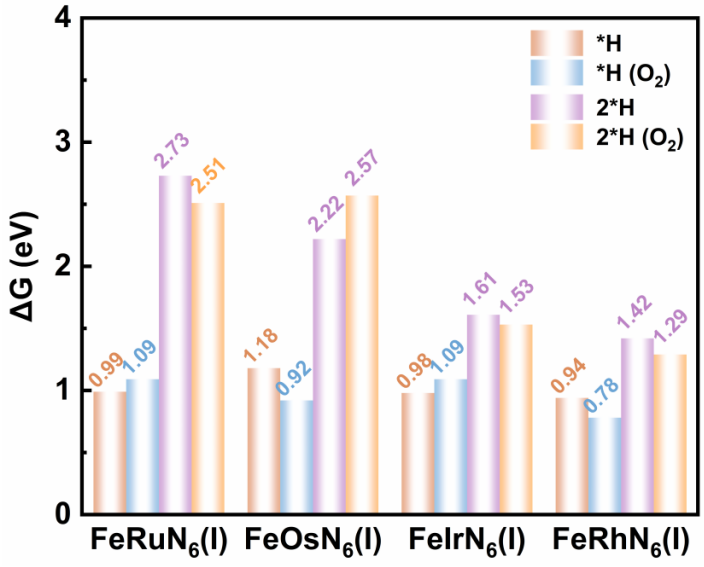


Figure 6. ΔG_{*H} and ΔG_{2*H} for $FeRuN_6$ (I), $FeOsN_6$ (I), $FeRhN_6$ (I), and $FeIrN_6$ (I).

Furthermore, since the structure of the reaction center is maintained after protonation and the interaction with one *H is flexible in the presence of O_2, a free energy diagram of ORR is simulated and compared with those of bare catalysts (Figure 7 and Table S7). It is shown that a small negative influence appears for the FeRh and FeIr pairs, and the overpotential becomes 0.54 V and 0.52 V, respectively. Attractively, the overpotentials for $FeRuN_6$(I) and $FeOsN_6$(I) become even lower than the bare metal centers, namely 0.35 V and 0.38 V, respectively, suggesting appealing acid performance.

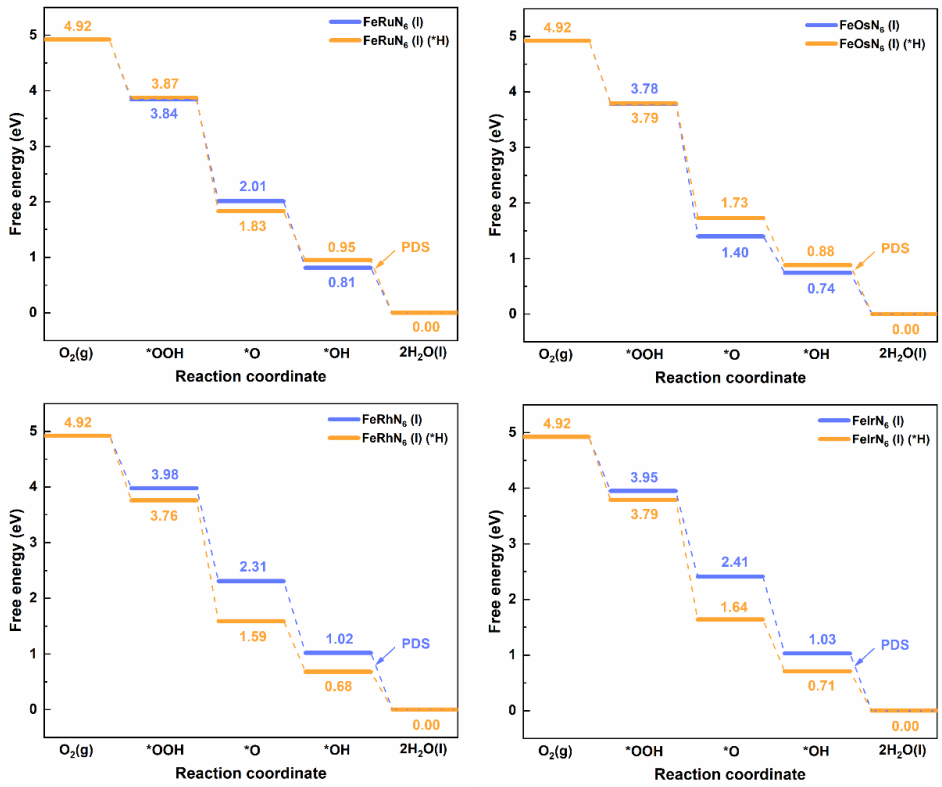


Figure 7. The free energy diagram of $FeRuN_6$ (I), $FeOsN_6$ (I), $FeRhN_6$ (I), and $FeIrN_6$ (I) with and without protonation.

3. Methodology

All the spin-polarized calculations were carried out by using the Vienna ab-initio simulation package (VASP) [36,37]. The Perdue–Burke–Enzerhof (PBE) [38] function and the projection-enhanced wave (PAW) [39] were used to describe the exchange-correlation potential and ion-electron interactions, respectively. The kinetic energy cut-off was set as 500 eV. A 5 × 5 supercell of graphene was used as the substrate for the diatomic centers. To avoid inter-layer interactions, a vacuum as large as 20 Å is set above the graphene slab. The dispersion correction for Van der Waals (vdW) [40] interactions was performed by the DFT-D2 [41] method. For structural optimization, a Γ centered 3 × 3 × 1 Monkhorst-Pack k-point sampling was used in the first Brillouin zone, which was increased to 7 × 7 × 1 for the electronic properties' calculations. The energy and force tolerance are 1×10^{-5} eV and 0.02 eV $Å^{-1}$, respectively [42,43]. For the assessment of kinetic stability, ab initio molecular dynamics (AIMD) [44] simulations were used, and the simulation time lasts 10 ps at 300 K.

The adsorption energy (ΔE_{ads}) was calculated as follows:

$$\Delta E_{ads} = E_{adsorbate+support} - (E_{adsorbate} + E_{support})$$

where $E_{adsorbate+support}$ is the total energy of the catalyst with the adsorbed intermediates, and $E_{adsorbate}$ and $E_{support}$ are the energy of the catalyst and the free adsorbate, respectively. The change of the Gibbs free energy (ΔG) was calculated via the computational hydrogen electrode (CHE) model [35]:

$$\Delta G = \Delta E_{ads} + \Delta E_{ZPE} - T\Delta S$$

where ΔE_{ZPE} and ΔS are the correction of zero-point energy and entropy, respectively. The free energy of O_2 (4.92 eV) was extracted from the reaction $O_2 + 2H_2 = 2H_2O$. The key elementary step for a 4e ORR pathway is as follows:

$$(R1)\ {}^*O_2 + H^+ + e \rightarrow {}^*OOH\ \Delta G_1 = \Delta G_{*OOH} - 4.92$$

$$(R2)\ {}^*OOH + H^+ + e \rightarrow {}^*O + H_2O\ \Delta G_2 = \Delta G_{*O} - \Delta G_{*OOH}$$

$$(R3)\ {}^*O + H^+ + e \rightarrow {}^*OH\ \Delta G_3 = \Delta G_{*OH} - \Delta G_{*O}$$

$$(R4)\ {}^*OH + H^+ + e \rightarrow H_2O\ \Delta G_4 = -\Delta G_{*OH}$$

Among them, the * denotes that the ORR species is adsorbed on the catalyst surface. The thermodynamic overpotential η [27,45] is thus determined by

$\eta = (1.23 - G/e)$ V wherein $G = \min\{|\Delta G_1|, |\Delta G_2|, |\Delta G_3|, |\Delta G_4|\}$.

In conclusion, a set of Fe-based dual metal site reaction centers supported by carbon have been studied using DFT calculations. Besides FeCo, FeMn, FeCu and FeZn pairs, which are available from experiments, FeIr (η = 0.26 V), FeRh (η = 0.30 V), FeRu (η = 0.42 V) and FeOs (η = 0.57 V) pairs are predicted with desirable ORR activity, which outperform even in an acid environment. AIMD simulations demonstrated their good structural stability at room temperature, providing new research directions for further catalytic design.

Supplementary Materials: The following supporting information can be downloaded at: https://www.mdpi.com/article/10.3390/catal13020418/s1, Figure S1: Gibbs free energy profiles for the designed catalysts.; Figure S2: Free energy diagram for FeTMN6(II) (TM = Cr, Mn, Mo, Ru, W, Re, Os, Co, Ni, CuRe, Os, Co, Ni, Cu, Zn, Rh and Ir) moieties; Figure S3: Energy evolution at 300 K for FeRuN6(I), FeOsN6(I), FeRhN6(I), and FeIrN6(I); Table S1: Structural evolution of electrochemical ORR for the designed catalysts, top view and side view; Table S1: Structural evolution of electrochemical ORR for the designed catalysts, top view and side view; Table S3: Bader charge (in units of e). Q(Fe), Q(Other) refer to the charge on Fe, other transition metals to DMSCs; Table S4: Adsorption free energies (ΔG*ads, eV) of the key ORR intermediate species associated with DMSCs; Table S5: O-O bond distance in $*O_2$, theoretical overpotential, half-wave potential ($E_{1/2}$) and onset potential (E_{onset}) in literature and this work; Table S6: Structural evolution of electrochemical ORR for DMSCs

with *H and 2*H, top view and side view; Table S7: Adsorption free energies (ΔG*ads, eV) of the key ORR intermediate species for DMSCs with *H and 2*H [22,26,28,29,46].

Author Contributions: Conceptualization, Y.W.; Formal analysis, Y.W., S.L., R.X. and Y.H.; Investigation, Y.W. and R.X.; Resources, Y.L. (Yingmei Li); Data curation, K.L.; Writing – original draft, Y.W.; Writing–review & editing, S.L., J.C. and Y.L. (Yingmei Li); Visualization, Y.L. (Yan Li); Supervision, Y.L. (Yingmei Li) and J.W.; Project administration, J.W.; Funding acquisition, J.W. All authors have read and agreed to the published version of the manuscript.

Funding: This research was funded by the Scientific Research Foundation for the Returned Overseas Chinese Scholars, Hebei Education Department (C20210503), Hebei provincial Department of Science and Technology (226Z4404G).

Data Availability Statement: Not applicable.

Acknowledgments: The authors are grateful for the resource from high performance computing center of Yanshan University.

Conflicts of Interest: The authors declare no conflict of interest.

References

1. Sun, W.; Wang, F.; Zhang, B.; Zhang, M.; Küpers, V.; Ji, X.; Theile, C.; Bieker, P.; Xu, K.; Wang, C.; et al. A rechargeable zinc-air battery based on Zinc peroxide chemistry. *Science* **2021**, *371*, 46–51. [CrossRef] [PubMed]
2. Wang, J.; Liu, W.; Luo, G.; Li, Z.; Zhao, C.; Zhang, H.; Zhu, M.; Xu, Q.; Wang, X.; Zhao, C.; et al. Synergistic effect of well-defined dual sites boosting the oxygen reduction reaction. *Energy Environ. Sci.* **2018**, *11*, 3375–3379. [CrossRef]
3. Lin, Z.Y.; Huang, H.; Cheng, L.; Hu, W.; Xu, P.P.; Yang, Y.; Li, J.M.; Gao, K.; Yang, F.Y.; Huang, M.X.; et al. Tuning the p-Orbital Electron Structure of s-Block Metal Ca Enables a High-Performance Electrocatalyst for Oxygen Reduction. *Adv. Mater.* **2021**, *33*, 2107103. [CrossRef] [PubMed]
4. Debe, M.K. Electrocatalyst approaches and challenges for automotive fuel cells. *Nature* **2012**, *486*, 43–51. [CrossRef]
5. Steele, B.C.; Heinzel, A. Materials for fuel-cell technologies. *Nature* **2001**, *414*, 345–352. [CrossRef]
6. Huang, S.; Lu, S.; Gong, S.; Zhang, Q.; Duan, F.; Zhu, H.; Gu, H.; Dong, W.; Du, M. Sublayer Stable Fe Dopant in Porous Pd Metallene Boosts Oxygen Reduction Reaction. *ACS Nano* **2021**, *16*, 522–532. [CrossRef]
7. Han, A.; Wang, X.; Tang, K.; Zhang, Z.; Ye, C.; Kong, K.; Hu, H.; Zheng, L.; Jiang, P.; Zhao, C.; et al. An adjacent atomic platinum site enables single-atom iron with high oxygen reduction reaction performance. *Angew. Chem. Int. Ed.* **2021**, *60*, 19262–19271. [CrossRef]
8. Qiao, B.; Wang, A.; Yang, X.; Allard, L.F.; Jiang, Z.; Cui, Y.; Liu, J.; Li, J.; Zhang, T. Single-Atom Catalysis of CO Oxidation Using Pt_1/FeO_x. *Nat. Chem.* **2011**, *3*, 634–641. [CrossRef]
9. Han, J.; Meng, X.; Lu, L.; Bian, J.; Li, Z.; Sun, C. Single-atom Fe-N_x-C as an efficient electrocatalyst for zinc-air batteries. *Adv. Funct. Mater.* **2019**, *29*, 1808872. [CrossRef]
10. Chen, G.; An, Y.; Liu, S.; Sun, F.; Qi, H.; Wu, H.; He, Y.; Liu, P.; Shi, R.; Zhang, J.; et al. Highly accessible and dense surface single metal FeN_4 active sites for promoting the oxygen reduction reaction. *Energy Environ. Sci.* **2022**, *15*, 2619–2628. [CrossRef]
11. Sarkar, S.; Biswas, A.; Siddharthan, E.E.; Thapa, R.; Dey, R.S. Strategic Modulation of Target-Specific Isolated Fe, Co Single-Atom Active Sites for Oxygen Electrocatalysis Impacting High Power Zn-Air Battery. *ACS Nano* **2022**, *16*, 7890–7903. [CrossRef] [PubMed]
12. Zhu, J.; Fang, Z.; Yang, X.; Chen, M.; Chen, Z.; Qiu, F.; Wang, M.; Liu, P.; Xu, Q.; Zhuang, X.; et al. Core-Shell Structured Fe-N-C Catalysts with Enriched Iron Sites in Surface Layers for Proton-Exchange Membrane Fuel Cells. *ACS Catal.* **2022**, *12*, 6409–6417. [CrossRef]
13. Zhang, H.; Hwang, S.; Wang, M.; Feng, Z.; Karakalos, S.; Luo, L.; Qiao, Z.; Xie, X.; Wang, C.; Su, D.; et al. Single atomic iron catalysts for oxygen reduction in acidic media: Particle size control and thermal activation. *J. Am. Chem. Soc.* **2017**, *139*, 14143–14149. [CrossRef] [PubMed]
14. Wang, J.; Li, H.; Liu, S.; Hu, Y.; Zhang, J.; Xia, M.; Hou, Y.; Tse, J.; Zhang, J.; Zhao, Y. Turning on Zn 4s Electrons in a N_2-Zn-B_2 Configuration to Stimulate Remarkable ORR Performance. *Angew. Chem. Int. Ed.* **2021**, *60*, 181–185. [CrossRef] [PubMed]
15. Zhao, C.-X.; Li, B.-Q.; Liu, J.-N.; Zhang, Q. Intrinsic Electrocatalytic Activity Regulation of M-N-C Single-Atom Catalysts for the Oxygen Reduction Reaction. *Angew. Chem. Int. Ed.* **2021**, *60*, 4448–4463. [CrossRef]
16. Sun, J.; Wang, N.; Qiu, Z.Z.; Xing, L.X.; Du, L. Recent Progress of Non-Noble Metal Catalysts for Oxygen Electrode in Zn-Air Batteries: A Mini Review. *Catalysts* **2022**, *12*, 843. [CrossRef]
17. Liu, J.; Wan, X.; Liu, S.; Liu, X.; Zheng, L.; Yu, R.; Shui, J. Hydrogen Passivation of M-N-C (M = Fe, Co) Catalysts for Storage Stability and ORR Activity Improvements. *Adv. Mater.* **2021**, *33*, 2103600. [CrossRef]
18. Tang, C.; Chen, L.; Li, H.; Li, L.; Jiao, Y.; Zheng, Y.; Xu, H.; Davey, K.; Qiao, S.-Z. Tailoring Acidic Oxygen Reduction Selectivity on Single-Atom Catalysts via Modification of First and Second Coordination Spheres. *J. Am. Chem. Soc.* **2021**, *143*, 7819–7827. [CrossRef]
19. Zhao, Q.; Wang, Y.; Lai, W.; Xiao, F.; Lu, Y.; Liao, C.; Shao, M. Approaching a high rate and sustainable production of hydrogen peroxide: Oxygen reduction on Co-N-C single-atom electrocatalysts in simulated seawater. *Energy Environ. Sci.* **2021**, *14*, 5444–5456. [CrossRef]

20. Yang, Z.; Chen, B.; Chen, W.; Qu, Y.; Zhou, F.; Zhao, C.; Xu, Q.; Zhang, Q.; Duan, X.; Wu, Y. Directly transforming copper (I) oxide bulk into isolated single-atom copper sites catalyst through gas-transport approach. *Nat. Commun.* **2019**, *10*, 3734. [CrossRef]
21. Ying, Y.; Luo, X.; Qiao, J.; Huang, H. "More is Different:" Synergistic Effect and Structural Engineering in Double-Atom Catalysts. *Adv. Funct. Mater.* **2021**, *31*, 2007423. [CrossRef]
22. Sun, H.; Wang, M.; Zhang, S.S.; Liu, S.; Shen, X.; Qian, T.; Niu, X.; Xiong, J.; Yan, C. Boosting Oxygen Dissociation over Bimetal Sites to Facilitate Oxygen Reduction Activity of Zinc-Air Battery. *Adv. Funct. Mater.* **2021**, *31*, 2006533. [CrossRef]
23. Wang, J.; Liu, C.; Li, S.; Li, Y.; Zhang, Q.; Peng, Q.; Tse, J.S.; Wu, Z. Advanced electrocatalysts with Dual-metal doped carbon Materials: Achievements and challenges. *Chem. Eng. J.* **2022**, *428*, 132558. [CrossRef]
24. Wan, W.; Zhao, Y.; Wei, S.; Triana, C.A.; Li, J.; Arcifa, A.; Allen, C.S.; Cao, R.; Patzke, G.R. Mechanistic insight into the active centers of single/dual-atom Ni/Fe-based oxygen electrocatalysts. *Nat. Commun.* **2021**, *12*, 1–13. [CrossRef]
25. Yang, G.; Zhu, J.; Yuan, P.; Hu, Y.; Qu, G.; Lu, B.-A.; Xue, X.; Yin, H.; Cheng, W.; Cheng, J.; et al. Regulating Fe-spin state by atomically dispersed Mn-N in Fe-N-C catalysts with high oxygen reduction activity. *Nat. Commun.* **2021**, *12*, 1–10. [CrossRef]
26. Wang, J.; Huang, Z.; Liu, W.; Chang, C.; Tang, H.; Li, Z.; Chen, W.; Jia, C.; Yao, T.; Wei, S. Design of N-coordinated dual-metal sites: A stable and active Pt-free catalyst for acidic oxygen reduction reaction. *J. Am. Chem. Soc.* **2017**, *139*, 17281–17284. [CrossRef] [PubMed]
27. Sun, Y.; Wang, J.; Liu, Q.; Xia, M.; Tang, Y.; Gao, F.; Hou, Y.; Tse, J.; Zhao, Y. Itinerant ferromagnetic half metallic cobalt-iron couples: Promising bifunctional electrocatalysts for ORR and OER. *J. Mater. Chem. A* **2019**, *7*, 27175–27185. [CrossRef]
28. Li, H.; Wang, J.; Qi, R.; Hu, Y.; Zhang, J.; Zhao, H.; Zhang, J.; Zhao, Y. Enhanced Fe 3d delocalization and moderate spin polarization in FeNi atomic pairs for bifunctional ORR and OER electrocatalysis. *Appl. Catal. B Environ.* **2021**, *285*, 119778. [CrossRef]
29. Li, H.; Di, S.; Niu, P.; Wang, S.; Wang, J.; Li, L. A durable half-metallic diatomic catalyst for efficient oxygen reduction. *Energy Environ. Sci.* **2022**, *15*, 1601–1610. [CrossRef]
30. Xiao, M.; Chen, Y.; Zhu, J.; Zhang, H.; Zhao, X.; Gao, L.; Wang, X.; Zhao, J.; Ge, J.; Jiang, Z.; et al. Climbing the apex of the ORR volcano plot via binuclear site construction: Electronic and geometric engineering. *J. Am. Chem. Soc.* **2019**, *141*, 17763–17770. [CrossRef]
31. Wang, J.; Xu, R.; Sun, Y.; Liu, Q.; Xia, M.; Li, Y.; Gao, F.; Zhao, Y.; John, S.T.; Zhao, Y. Identifying the Zn-Co binary as a robust bifunctional electrocatalyst in oxygen reduction and evolution reactions via shifting the apexes of the volcano plot. *J. Energy Chem.* **2021**, *55*, 162–168. [CrossRef]
32. Deng, C.; Su, Y.; Li, F.; Shen, W.; Chen, Z.; Tang, Q. Understanding activity origin for the oxygen reduction reaction on bi-atom catalysts by DFT studies and machine-learning. *J. Mater. Chem. A* **2020**, *8*, 24563–24571. [CrossRef]
33. Yu, Z.; Si, C.; LaGrow, A.P.; Tai, Z.; Caliebe, W.A.; Tayal, A.; Sampaio, M.J.; Sousa, J.P.; Amorim, I.; Araujo, A.J.; et al. Iridium-Iron Diatomic Active Sites for Efficient Bifunctional Oxygen Electrocatalysis. *ACS Catal.* **2022**, *12*, 9397–9409. [CrossRef]
34. Li, K.; Li, Y.; Peng, W.C.; Zhang, G.L.; Zhang, F.B.; Fan, X.B. Bimetallic Iron–Cobalt Catalysts and Their Applications in Energy-Related Electrochemical Reactions. *Catalysts* **2019**, *9*, 762. [CrossRef]
35. Sabatier, P. *La Catalyse en Chimie Organique*; Librairie Polytechnique: Paris, France, 1920.
36. Kresse, G.; Furthmuller, J. Efficient iterative schemes for ab initio total-energy calculations using a plane-wave basis set. *Phys. Rev. B* **1996**, *54*, 11169–11186. [CrossRef]
37. Kresse, G.; Furthmuller, J. Efficiency of ab-initio total energy calculations for metals and semiconductors using a plane-wave basis set, Computational Materials. *Science* **1996**, *6*, 15–50.
38. Blöchl, P.E. Projector augmented-wave method. *Phys. Rev. B* **1994**, *50*, 17953–17979. [CrossRef]
39. Perdew, J.P.; Burke, K.; Ernzerhof, M. Generalized Gradient Approximation Made Simple. *Phys. Rev. Lett.* **1996**, *77*, 3865–3868. [CrossRef]
40. Grimme, S. Semiempirical GGA-type density functional constructed with a long-range dispersion correction. *J. Comput. Chem.* **2006**, *27*, 1787–1799. [CrossRef]
41. Grimme, S.; Antony, J.; Ehrlich, S.; Krieg, H. A consistent and accurate ab initio parametrization of density functional dispersion correction (DFT-D) for the 94 elements H-Pu. *J. Chem. Phys.* **2010**, *132*, 154104. [CrossRef]
42. Monkhorst, H.J.; Pack, J.D. Special points for Brillouin-zone integrations. *Phys. Rev. B* **1976**, *13*, 5188–5192. [CrossRef]
43. Govind, N.; Petersen, M.; Fitzgerald, G.; King-Smith, D.; Andzelm, J. A generalized synchronous transit method for transition state location. *Comput. Mater. Sci.* **2003**, *28*, 250–258. [CrossRef]
44. Norskov, J.K.; Rossmeisl, J.; Logadottir, A.; Lindqvist, L.; Kitchin, J.R.; Bligaard, T.; Jonsson, H. Origin of the overpotential for oxygen reduction at a fuel-cell cathode. *J. Phys. Chem. B* **2004**, *108*, 17886–17892. [CrossRef]
45. Li, X.Y.; Duan, S.; Sharman, E.; Zhao, Y.; Yang, L.; Zhuo, Z.W.; Cui, P.; Jiang, J.; Luo, Y. Exceeding the volcano relationship in oxygen reduction/evolution reactions using single-atombased catalysts with dual-active-sites. *J. Mater. Chem. A* **2020**, *8*, 10193–10198. [CrossRef]
46. Han, X.; Ling, X.; Yu, D.; Xie, D.; Li, L.; Peng, S.; Zhong, C.; Zhao, N.; Deng, Y.; Hu, W. Atomically Dispersed Binary Co-Ni Sites in Nitrogen-Doped Hollow Carbon Nanocubes for Reversible Oxygen Reduction and Evolution. *Adv. Mater.* **2019**, *31*, e1905622. [CrossRef]

Disclaimer/Publisher's Note: The statements, opinions and data contained in all publications are solely those of the individual author(s) and contributor(s) and not of MDPI and/or the editor(s). MDPI and/or the editor(s) disclaim responsibility for any injury to people or property resulting from any ideas, methods, instructions or products referred to in the content.